

Reaction pathways of BCl_3 for acceptor delta-doping of silicon

Quinn Campbell,^{1, a)} Kevin J. Dwyer,^{2, b)} Sungha Baek,² Andrew D. Baczewski,¹ Robert E. Butera,^{3, c)} and Shashank Misra⁴

¹⁾*Center for Computing Research, Sandia National Laboratories, Albuquerque NM 87185*

²⁾*Department of Physics, University of Maryland, College Park, MD 20742*

³⁾*Laboratory for Physical Sciences, College Park, MD 20740*

⁴⁾*Sandia National Laboratories, Albuquerque NM 87185*

(Dated: 28 January 2022)

BCl_3 is a promising candidate for atomic-precision acceptor doping in Si, but optimizing the electrical properties of structures created with this technique requires a detailed understanding of adsorption and dissociation pathways for this precursor. Here, we use density functional theory and scanning tunneling microscopy (STM) to identify and explore these pathways for BCl_3 on Si(100) at different annealing temperatures. We demonstrate that BCl_3 adsorbs selectively without a reaction barrier, and subsequently dissociates relatively easily with reaction barriers ≈ 1 eV. Using this dissociation pathway, we parameterize a Kinetic Monte Carlo model to predict B incorporation rates as a function of dosing conditions. STM is used to image BCl_3 adsorbates, identifying several surface configurations and tracking the change in their distribution as a function of the annealing temperature, matching predictions of the kinetic model well. This straightforward pathway for atomic-precision acceptor doping helps enable a wide range of applications including bipolar nanoelectronics, acceptor-based qubits, and superconducting Si.

^{a)}Electronic mail: qcampbe@sandia.gov; Q.C. and K.D. contributed equally to this work

^{b)}Q.C. and K.D. contributed equally to this work

^{c)}Electronic mail: rbutera@lps.umd.edu

I. INTRODUCTION

Atomic precision advanced manufacturing (APAM) techniques are essential for the realization of a wide variety of novel quantum and electronic devices in Si such as dopant-based qubits,^{1,2} analog quantum simulators,³ and superconducting devices.⁴ APAM utilizes a Si surface that has been passivated with a monatomic resist such as H or Cl.⁵⁻⁷ A precision lithography tool in the form of a scanning tunneling microscope (STM) is then used to de-passivate a region of interest^{8,9} that selectively reacts with a gaseous molecular precursor in ultrahigh vacuum (UHV). Under appropriate conditions, the precursor will fully dissociate on the surface and ultimately incorporate a dopant atom into the Si substrate. The carrier density achieved with APAM can readily exceed $1 \times 10^{14} \text{ cm}^{-2}$, creating well-defined, quasi-2D δ -doped regions within Si.¹⁰ To date, APAM process development has focused almost exclusively on the formation of P-based devices using phosphine (PH_3) as the dopant precursor.¹¹⁻¹³ However, the pursuit of APAM-compatible acceptor doping has gained interest for creating bipolar electronic devices,¹⁴ enabling qubits with high intrinsic spin-orbit coupling,¹⁵⁻¹⁷ and the possibility of creating superconducting regions within Si.^{4,18-20}

Recent work has explored a variety of potential APAM-compatible acceptor precursors such as diborane (B_2H_6),¹⁴ aluminum trichloride (AlCl_3),²¹ boron trichloride (BCl_3),²² and organics such as trimethyl and triethyl aluminum²³. Additionally, several solution-based approaches have been explored.²⁴⁻²⁸ Of these, BCl_3 in UHV has shown the most promise for δ -doping applications, achieving an active carrier concentration of $1.9 \times 10^{14} \text{ cm}^{-2}$ without the need of subsequent thermal processing.²² Moreover, BCl_3 has been shown to be compatible with both H and Cl resists, enabling the fabrication of B-doped APAM nanowires²² and fostering compatibility with PH_3 to create bipolar devices.¹⁴ Further optimization of the BCl_3 doping process is likely to be achieved by fine-tuning the dosing and anneal parameters to maximize both dopant incorporation and activation. Consequently, a detailed understanding of the reaction pathways and kinetics can identify possible routes for improving incorporation results, and further understanding differences from the analogous process in PH_3 in creating devices. This is particularly important in the context of achieving deterministic single-dopant incorporation.²⁹

In this work, we use Density Functional Theory (DFT) to elucidate the adsorption and dissociation pathway for BCl_3 on $\text{Si}(100)\text{-}2\times 1$. We demonstrate that BCl_3 adsorbs dissocia-

tively onto the surface in a barrierless process, creating high levels of selectivity with both H and Cl resists. Further dissociation occurs with barriers that are easily overcome near room temperature. We feed these barriers into a Kinetic Monte Carlo (KMC) model to predict B incorporation levels as a function of dose temperature. This contrasts with earlier work with phosphine which shows a several step dissociation pathway and higher reaction barriers for full dissociation.³⁰ STM is also used to observe adsorbed BCl_3 -related species (BCl_x with $x = 1$ to 3) on a Si(100) surface before and after annealing, with changes in surface structures found to be in good agreement with the dissociation behavior predicted by the model. This work further confirms BCl_3 to be an ideal acceptor precursor for APAM processes with these refinements pointing the way toward room-temperature fabrication of bipolar nanoelectronic devices,¹⁴ acceptor based qubits,¹⁵ and superconducting regions within Si.¹⁸

II. METHODS

A. Electronic Structure Calculations

We determine the thermodynamic adsorption energy of any particular BCl_x -surface configuration using DFT with the following equation:

$$E_a = E_{\text{slab}/\text{BCl}_3} - E_{\text{slab}} - E_{\text{BCl}_3}, \quad (1)$$

where E_a is the adsorption energy of the molecule on the Si surface, $E_{\text{slab}/\text{BCl}_3}$ is the total energy of the adsorbate on the slab, E_{slab} is the total energy of the slab without any adsorbate, and E_{BCl_3} is the total energy of the isolated BCl_3 molecule. Negative values of E_a imply a thermodynamically favorable adsorption energy for that configuration. All energy calculations are performed using the plane wave QUANTUM-ESPRESSO software package.³¹ To compute reaction barriers between configurations, we use the Nudged Elastic Band (NEB) method, also implemented in QUANTUM-ESPRESSO, and use norm-conserving pseudopotentials from the PseudoDojo repository³² and the Perdew-Burke-Ernzerhof exchange correlation functional.³³ Kinetic energy cutoffs of 50 Ry and 200 Ry are used for the plane wave basis sets used to describe the Kohn-Sham orbitals and charge density, respectively, and a $2 \times 2 \times 1$ Monkhorst-Pack grid is used to sample the Brillouin zone.³⁴

Adsorption energy calculations are performed on the 4×4 supercell of a seven-layer thick Si(100)- 2×1 slab with a 20 Å vacuum region, where a single unit cell has a size of $3.87 \text{ Å} \times$

3.87 Å. Matching the experimentally measured Si structure, we model the Si surface with alternating buckled Si dimers. A H resist is placed on the surface with the exception of three Si dimer sites to gauge the selectivity of BCl₃ molecules on a bare Si surface versus a passivated surface. On the other end of the slab, the Si dangling bonds are passivated with Se atoms to prevent spurious surface effects. The bottom four layers of the slab are frozen and the geometry of the surface layers along with the adsorbate are relaxed until the interatomic forces are lower than 50 meV/Å. We compute the reference molecular energy for a single BCl₃ molecule in a 15 Å³ box.

B. Kinetic Monte Carlo

A KMC model^{35,36} implemented using the KMCLib software package³⁷ is used to predict the incorporation rate of B atoms in patches of exposed Si(100) several nanometers wide. Our KMC model uses transition rates based on the Arrhenius equation $\Gamma = A \exp \Delta/k_B T$,³⁸ where Γ is transition rate, A is the attempt frequency, Δ is the reaction barrier found from our earlier DFT calculations, k_B is the Boltzmann constant, and T is the temperature. Attempt frequencies are set to 10¹² s⁻¹ as a reasonable order of magnitude estimate based on an analysis of attempt frequencies for the dissociation of PH₃ on Si.³⁰

We calculate the effusive flow rate of molecules landing on any particular Si dimer as $\Phi_{effusion} = Pa/\sqrt{2\pi mk_B T}$, where P is the pressure of the incoming precursor gas, a is the area of impingement, taken here as a single Si dimer, m is the mass of the precursor gas, k_B is the Boltzmann constant, and T is the temperature.

Each KMC calculation is repeated 200 times to obtain a meaningful statistical sampling of likely outcomes and we report the average outcomes, along with standard deviations as applicable. We calculate the standard error by assuming a Poisson distribution of measured counts. For ease of reproducibility, we have placed our KMC code on github.³⁹

C. Si Surface Preparation

BCl₃ dosing, annealing, STM imaging (ZyVector STM Lithography controller), and δ -layer fabrication were performed in a ScientaOmicron VT-STM UHV system with base pressure $P < 2.7 \times 10^{-9}$ Pa (2.0×10^{-11} Torr). Si(100) wafers used in these experiments

were p-type (B-doped) obtained from ITME with resistivity $\rho = 1 \text{ } \Omega\cdot\text{cm}$ to $10 \text{ } \Omega\cdot\text{cm}$. Samples $4 \text{ mm} \times 12 \text{ mm}$ in size were cleaned by sonication in acetone, methanol, and isopropanol before being loaded into the UHV system on a ScientaOmicron XA sample plate. Clean Si(100)-(2 \times 1) surfaces were prepared in UHV by rapidly annealing the samples to 1225°C via Joule heating before being scanned in the STM for contaminants, as described elsewhere.²²

D. BCl_3 Dosing and δ -Layer Fabrication

Si(100) samples were dosed with BCl_3 within the UHV system immediately after initial annealing to form a clean surface. A precision leak valve was used to introduce BCl_3 into the UHV chamber and expose samples to a 1.5 langmuir dose ($1 \text{ langmuir} = 10^{-6} \text{ Torr}\cdot\text{s}$) at room temperature ($\approx 20^\circ\text{C}$) using a dosing pressure of $4.0 \times 10^{-9} \text{ Torr}$. The samples were then imaged with STM both before and after anneals at different temperatures ranging from 250°C to 600°C . STM image processing and statistical analysis of adsorbates were performed using Gwyddion⁴⁰ to get feature coverages, reported in monolayers (ML), where 1 ML is equivalent to the Si(100) dangling bond density ($6.78 \times 10^{14} \text{ cm}^{-2}$).

E. Electrical Characterization

Electrical properties of B δ -layer samples were determined using standard Hall bar magnetotransport measurements in a Quantum Design Physical Property Measurement System (PPMS). The Hall bars were patterned using electron beam lithography and were etched by a reactive ion etcher (RIE), as described elsewhere.²² We created ohmic contacts using wire-bonding on mesa-defined pads. Each pad contained a 50×50 array of $1 \text{ } \mu\text{m}$ sized etched squares and were wire-bonded with Al wires using a West Bond 7476E with a power of 300 W and a 30 ms time constant.

To study electrical carrier properties, samples were measured at 3 K while a magnetic field was applied perpendicular to the sample surface and swept from -2.5 T to $+2.5 \text{ T}$. Four-terminal resistances were measured using an AC current source to apply $2 \text{ } \mu\text{A}$ for longitudinal voltage measurements and $10 \text{ } \mu\text{A}$ for transverse voltage measurements.

III. RESULTS AND DISCUSSION

The thermodynamic reaction pathway for BCl_3 decomposing on a $\text{Si}(100)\text{-}2\times 1$ surface was determined using DFT, with the lowest energy configurations shown in Fig. 1(a). A BCl_3 molecule adsorbs dissociatively onto the Si surface, with one Cl splitting off to one side of the Si dimer and the remaining BCl_2 bonding to the other side of the dimer (configuration A). Atomic positions for Si (blue), B (dark green), and Cl (light green) are shown for configuration A with the BCl_2 fragment residing over the dimer row. This initial reaction has an adsorption energy of -1.74 eV, indicating significantly stronger adsorption than is seen for PH_3 and B_2H_6 , which have adsorption energies of around -0.70 eV to -0.90 eV.^{30,41} This initial adsorption energy agrees well with recent theoretical work⁴² which estimates the BCl_3 adsorption energy on bare $\text{Si}(100)$ to be -1.76 eV and matches previously predicted BCl_3 adsorption configurations.⁴³ Furthermore, the adsorption has no reaction barrier, implying a sticking coefficient of ≈ 1 . This correlates well with previous experiments that have demonstrated room temperature adsorption of BCl_3 on Si.^{22,44–46} This high adsorption energy can largely be attributed to the dissociation of BCl_3 and the formation of a strong Si-Cl bond: when BCl_3 bonds non-dissociatively on a bare Si surface, we calculate an adsorption energy of only -0.28 eV. We also predict BCl_3 to be highly selective on both H and Cl resists, with an adsorption energy of -0.03 eV and -0.02 eV, respectively, corresponding to weak physisorption and matching previous reports of BCl_3 selectivity on these resists.²² This matches predictions that all chemical bonding configurations on the Si-Cl surface require overcoming significant reaction barriers of ≈ 2 eV.⁷

From this initial configuration, the BCl_2 fragment can proceed along one of two possible directions: losing a Cl to a nearby Si dimer (configuration B in Fig. 1), or moving directly to a BCl fragment bridging two neighboring Si dimers while a Cl moves to the opposite end of the neighboring dimer (configuration C). Configuration B is metastable with an adsorption energy of -0.76 eV, and requires overcoming a 1.04 eV barrier from configuration A to move into, as shown in Fig. 1(b). In contrast, configuration C is highly stable with an adsorption energy of -2.18 eV. Atomic positions for configuration C are also shown indicating the BCl fragment protrudes out between dimer rows. Moving directly from configuration A to C has a barrier of 0.93 eV, implying that it will be more kinetically favorable for a BCl_2 fragment to move straight from configuration A to C instead of moving through the intermediate B

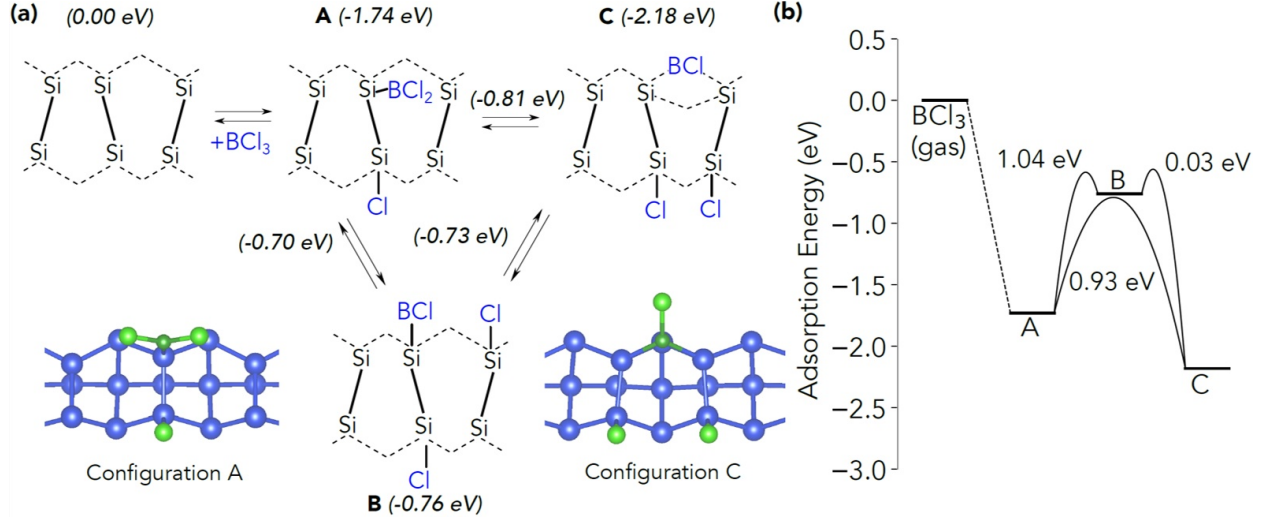


FIG. 1. (a) The reaction pathway of BCl_3 on a Si(100) surface. The numbers in parenthesis represent the adsorption energy of the configuration or the transition state (arrows). The BCl_3 initially adsorbs without a barrier onto a single Si dimer, splitting so that BCl_2 takes up one side of the dimer and a Cl moves to the other side (configuration A). The remaining Cl atoms are eventually shed until reaching configuration C where BCl bridges between two dimers, which we assume will lead to an eventual B incorporation. Configuration B is metastable. Si (blue), B (dark green), and Cl (light green) atomic positions are shown for configurations A and C. (b) The energetic pathway for adsorption.

state. This reaction pathway significantly resembles the previously elucidated pathway for AlCl_3 , although the reaction barriers are $\approx 0.3 \text{ eV}$ higher.²¹

Overall, the reaction pathway is both straightforward in contrast with similar reaction pathways for PH_3 and B_2H_6 ,^{30,41} and thermodynamically downhill. This pathway implies that if sufficient thermal energy is applied, a BCl_3 molecule can adsorb and move into a stable bridging configuration with no obstacles.

To predict the rate of B incorporation into a Si(100) surface as a function of the dose and annealing conditions (i.e. pressure, temperature, time), we use a KMC model based on our calculated reaction pathway. We additionally include desorption reactions for configuration A, B, and C, although due to the high adsorption energy, these do not occur at low temperatures. Given the highly stable adsorption energy of the bridging BCl fragment (configuration C) and the significant reaction barrier to reversing the dissociation (1.37 eV), it is highly unlikely that it will be ejected from the surface in subsequent steps. Within

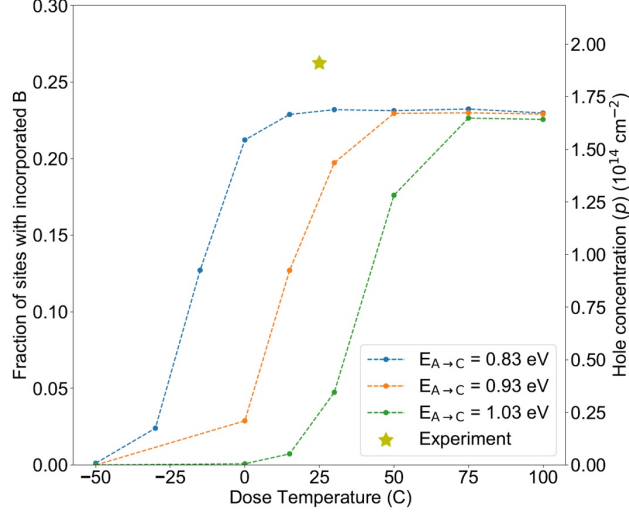


FIG. 2. KMC simulations of the incorporation fraction of BCl_3 on a $5 \text{ nm} \times 5 \text{ nm}$ patch of bare $\text{Si}(100)$ for various dose temperatures. We examine multiple values for the main barrier in the dissociation pathway (configuration A to C in Fig. 1). In all cases, saturation is achieved at relatively low temperatures ($<100^\circ\text{C}$). Also shown is an experimental value (star) of the measured hole concentration (p) for a δ -layer sample dosed at room temperature (i020).

our kinetic model, we therefore consider reaching the bridging BCl fragment to be an incorporation event. While this ignores subsequent steps of the incorporation process, previous kinetic models for PH_3 and B_2H_6 using analogous incorporation proxies of bridging PH and BH fragments have shown good agreement with experimental measures of incorporation.^{29,41} Based on the simplicity of the predicted reaction pathway and the low reaction barriers in the previous section, we expect that BCl_3 would lead to high levels of incorporation without the need for high temperatures.

Figure 2 shows the kinetic model’s predictions of the fraction of surface sites with incorporated B (bridging BCl) as a function of dose temperature. This intuition is matched in our predicted results of incorporation in δ -layer, with high incorporation rates occurring near room temperature with only minimal heating. The onset temperature at which incorporation begins is highly dependent on the main reaction in the pathway connecting configuration A to C, as shown in Fig. 1. Given that DFT reaction barriers are likely only accurate to $\pm 0.1 \text{ eV}$, we investigate the impact of raising or lowering the barrier by 0.1 eV . For the previously calculated barrier (0.93 eV) the system reaches saturation of incorporated B (corresponding to roughly 0.25 ML of coverage) at a little over room temperature

($\approx 40^\circ\text{C}$). This saturation temperature increases to roughly 75°C if the A to C barrier is increased to 1.03 eV, and it decreases to 0°C in the case of the barrier being lowered to 0.83 eV. While there is significant variation in the exact onset temperature, saturation is achieved in all three cases at $<100^\circ\text{C}$, a strong contrast to B_2H_6 and to a lesser extent PH_3 . The predictions in Fig. 2 are compared to an experimental value (star) of the hole concentration (p) for a sample dosed with BCl_3 at room temperature and not annealed measured using Hall bar magnetotransport measurements.

To verify the KMC predictions, STM was used to investigate the evolution of BCl_x species adsorbed on the Si(100) surface as a function of annealing temperature. Figure 3 shows filled-state STM images of clean Si(100) surfaces after BCl_3 dosing and annealing in UHV. A surface dosed with 1.5 langmuir BCl_3 at room temperature is shown in (a) and is representative of all dosed samples before annealing. Numerous bright BCl_x adsorbates are observed both on and between Si dimer rows, which are marked with dashed lines in the inset of (a). The DFT calculations suggest BCl_3 dissociatively adsorbs onto the surface at room temperature in a barrierless process, and the variety of larger and smaller adsorbate features observed in Fig. 3(a) support this notion. The saturation dose used here results in a surface coverage of adsorbates of 0.26(1) ML at room temperature. Figure 3(d-i) show dosed surfaces after annealing at 250°C , 350°C , 400°C , 450°C , 500°C , and 600°C , respectively, revealing that as the annealing temperature is increased, the amount of bright adsorbates is visibly reduced.

Figure 3(b) shows the surface coverage of BCl_x adsorbates (circles), surface defects (squares), and Si chains (triangles) for each annealing temperature. At 250°C , the surface coverage of BCl_x remains similar to that after dosing at room temperature (0.26(1) ML). However, above 250°C the BCl_x coverage drops linearly to just 0.11(2) ML at 500°C . This reduction is likely due to a combination of factors including desorption of BCl_2 fragments, as predicted by the model for temperatures above 250°C , as well as incorporation of B into the surface. We note that the appearance of some surface features are potentially due to subsurface B atoms rather than BCl_x adsorbates.⁴⁷ At 600°C , the surface features became more ambiguous and were ignored in the coverage plot. Above 350°C , short Si chains appear along with an increase in dark dimer defects, as seen in Fig. 3(h, i) and plotted in Fig. 3(b). Some defects can be attributed to Cl atoms on the surface shed from BCl_3 , but appear too similar to other defects to distinguish here. However, additional surface vacancy defects are

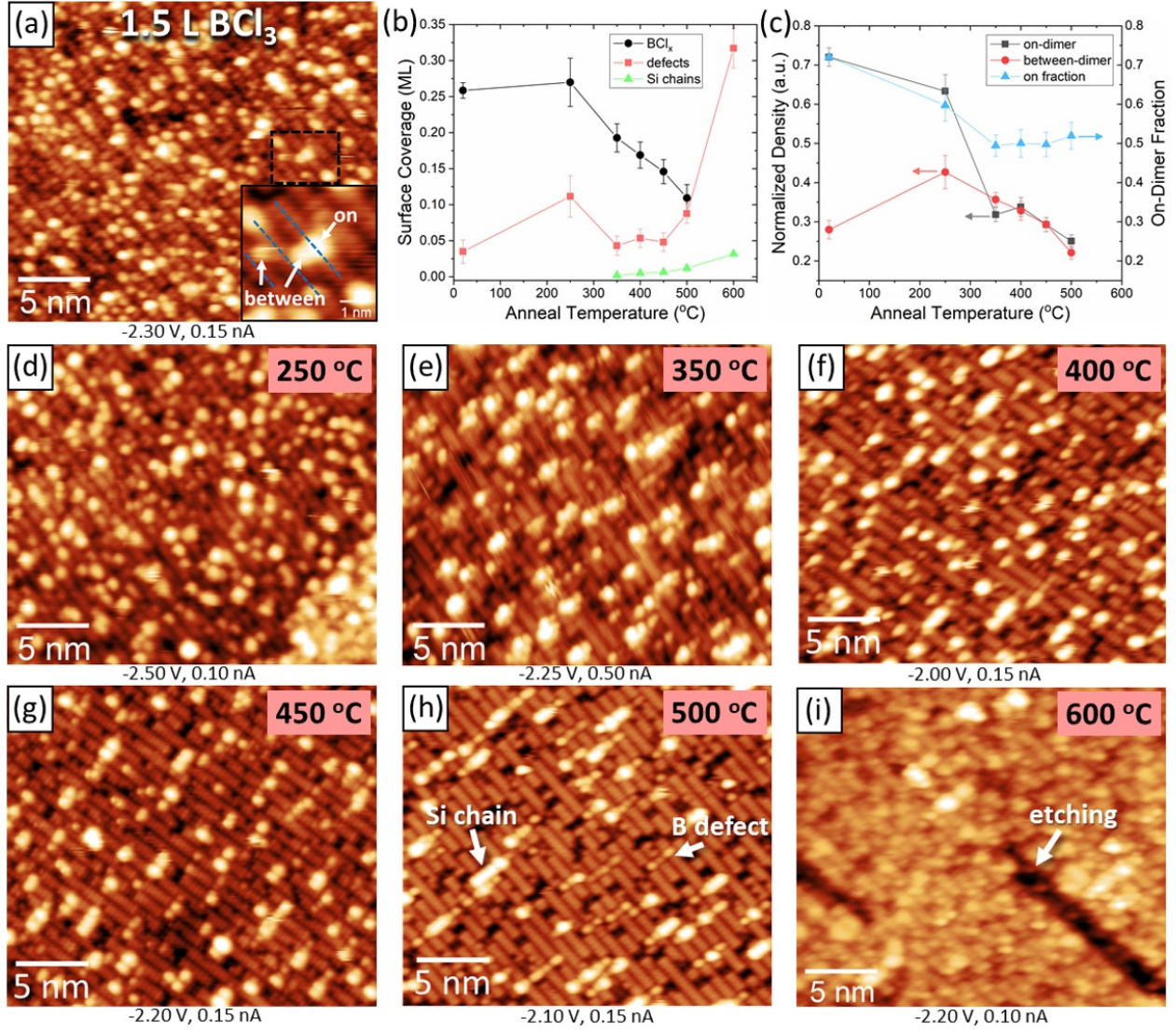


FIG. 3. Filled-state STM images of a Si(100) surface (a) dosed with 1.5 langmuir BCl_3 at room temperature and similar surfaces after annealing at (d) 250 °C, (e) 350 °C, (f) 400 °C, (g) 450 °C, (h) 500 °C, and (i) 600 °C. The inset of (a) magnifies the dashed box area and shows adsorbate features on and between dimer rows (dashed lines). At 500 °C, Si chains and three-dimer-wide “B defect” features are observed (arrows), indicating B incorporation, and Cl etching is apparent at 600 °C. (b) The surface coverage of BCl_x adsorbates (circles), surface defects (squares), and Si chains (triangles) versus annealing temperature. Adsorbate coverage decreases with increasing temperature while defects and Si chains increase. (c) The normalized density of BCl_x species (left axis) versus annealing temperature with on-dimer features (squares) converting to between dimers (circles). The on-dimer fraction (triangles, right axis) is also shown. Error bars are the standard error of feature counts.

likely caused by Cl on the surface which then etches Si⁴⁸ and is more pronounced at 600 °C in Fig. 3(i).

The appearance of Si chains can indicate ejected Si due to B incorporation. Here, short Si chains first appear at 350 °C, and longer ones are evident at 500 °C (Fig. 3(h)) and 600 °C (not shown) with a coverage of 0.032(2) ML at 600 °C. Unlike for P incorporation from PH₃ dosing, the Si chain coverage cannot give an accurate count of incorporated B due to the Cl etching and roughening process. B incorporation is also evidenced by the three-dimer-wide “B defect” features identified in Fig. 3(h) likely related to subsurface B, which is known to form similar defects in highly B-doped Si(100) substrates.^{47,49} Annealing at 1000 °C leads to further B incorporation and diffusion into the surface causing the formation of the known “bowtie” appearance, affirming bulk-like B incorporation (see Supplementary Material).

To further compare the predicted incorporation path of the KMC model to experiment, STM images were analyzed to determine on-dimer and between-dimer feature statistics. From Fig. 1(a), BCl₂ fragments are expected to reside on one side of a dimer row (configuration A), while BCl is expected to protrude between dimer rows (configuration C). Simulated STM images of these two configurations indicate that both configuration A and C would appear as several distinct features (see Supplementary Material) with A consisting of a pair of bright features (BCl₂) on the dimer row and C consisting of several features (Cl) on the dimer row as well as a feature (BCl) centered between rows. As predicted by the model, 0.56 of the total B on the surface should reside in configuration C at room temperature, and so we estimate that ≈ 0.74 of the total features are expected to reside on dimer rows with ≈ 0.26 of the features being between rows. Figure 3(c) plots the on-dimer (squares) and between-dimer (circles) density of features at each annealing temperature (left axis). The values are normalized to the initial total coverage to account for the decrease in adsorbate coverage with temperature. Also shown are the on-dimer features as a fraction of the total (triangles, right axis). At room temperature (no anneal), we find that 0.72(1) of the total features reside on dimer rows, in good agreement with the fraction estimated from the model (0.74), while 0.28(1) of features are between dimers. Thus we associate configuration A with several on-dimer features and C with both on-dimer and between-dimer features.

Above 300 °C, the density of on-dimer features drops significantly to 0.32(2), similar to the between-dimer density. This drop can be attributed to a combination of BCl₂ desorption and full conversion of BCl₂ fragments in configuration A to BCl in C, predicted above 300 °C. The

on-dimer fraction remains constant at ≈ 0.5 at temperatures above 350 °C as configuration C contributes some on-dimer features (Cl) as well. The increase in the between-dimer features from 0.28(1) of the initial total at room temperature to 0.43(4) at 250 °C is also consistent with this interpretation.

While our proposed model has good agreement with experimental trends, there are still a number of factors that could be included for a more realistic picture of delta doping with BCl_3 . The model does not account for site blocking by other adsorbates from the vacuum. Additionally, the model only includes interactions along a Si dimer row, and not between rows. While this serves as a good first approximation, interaction between dimer rows could result in decreased incorporation rates by enabling Cl atoms to migrate to adjacent rows but not BCl_x fragments, thus limiting space on nearby rows for dissociation. Further, due to the increase in computational complexity, we have not considered any dissociation steps beyond the bridging BCl fragment. Nevertheless, the results in this work demonstrate that this simplified model works well as a first approximation of BCl_3 dissociation on the surface. This helps confirm our dissociation pathway which is drastically simplified in comparison with PH_3 .

IV. CONCLUSION

In this work, we elucidate the dissociation pathway for BCl_3 using DFT, observing that BCl_3 adsorbs dissociatively onto the Si(100) surface in a barrierless process, forming a strong Si-Cl bond. Based on this reaction pathway, we parameterize a KMC model and use it to predict incorporation rates as a function of dosing/annealing conditions. We predict BCl_3 can incorporate to levels nearing $\approx 1.7 \times 10^{14} \text{ cm}^{-2}$ with only room-temperature dosing and no further annealing step, corroborating this model with electrical transport measurements of BCl_3 -doped δ -layers. STM is used to image BCl_3 -dosed surfaces under these conditions, identifying surface structures and broadly verifying the predicted dissociation kinetics. This work demonstrates a straightforward, thermodynamically downhill dissociation pathway for BCl_3 which presents a unique set of characteristics for creating δ -doped layers in comparison with PH_3 . Our work creates a better understanding of BCl_3 characteristics for the creation of APAM-based bipolar devices, acceptor qubits, and superconducting regions within Si.

V. SUPPLEMENTARY MATERIAL

See the supplementary material/appendices for simulated STM images of BCl_x adsorbates and an experimental STM image of BCl_3 -dosed Si surface after incorporation at 1000 °C.

ACKNOWLEDGMENTS

The authors acknowledge S. Schmucker, J. Ivie, and J. Owen for useful discussions regarding modeling directions. The authors also thank J. Foglebach, D. Ketchum, P. Hannah, J. Moody, S. Brown and T. Olver for their assistance with BCl_3 handling and installation. Electrical measurements were supported by the Maryland Quantum Materials Center (facilities support).

This work was supported by the Laboratory Directed Research and Development program at Sandia National Laboratories under project 213017 (FAIR DEAL) and performed, in part, at the Center for Integrated Nanotechnologies, an Office of Science User Facility operated for the U.S. Department of Energy (DOE) Office of Science. Sandia National Laboratories is a multi-mission laboratory managed and operated by National Technology and Engineering Solutions of Sandia, LLC, a wholly owned subsidiary of Honeywell International, Inc., for DOE’s National Nuclear Security Administration under contract DE-NA0003525. This paper describes objective technical results and analysis. Any subjective views or opinions that might be expressed in the paper do not necessarily represent the views of the U.S. Department of Energy or the United States Government.

VI. DATA AVAILABILITY

The data that support the findings of this study are available within the article and its supplementary material or from the corresponding author upon reasonable request. KMC code used in this study is available on github.³⁹.

Appendix A: Simulated STM Images of BCl_x

After equilibrium geometries were calculated using DFT, we generated an STM output with a sample bias of -2.2 V using QUANTUM ESPRESSO post processing software. We

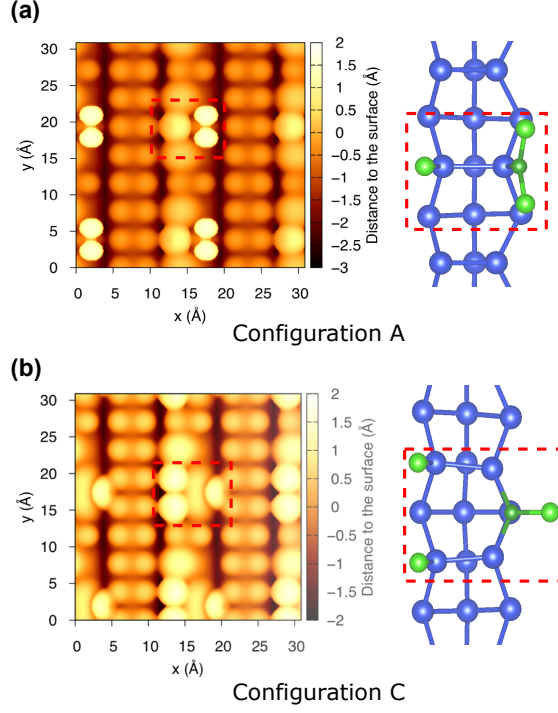


FIG. 4. Simulated STM images of (a) configuration A and (b) configuration C, as labeled in Fig. 1 (main text). STM images are generated with a bias of -2.2 V. The dotted red box shows the correspondence between the atomic structure and the STM feature.

then use the CRITIC2 software package⁵⁰ to generate the simulated constant current STM images with a threshold of 0.00005 atomic units of a 2×2 supercell of the simulated surface.

Appendix B: STM of BCl_3 -Dosed Si(100) Annealed at 1000°C

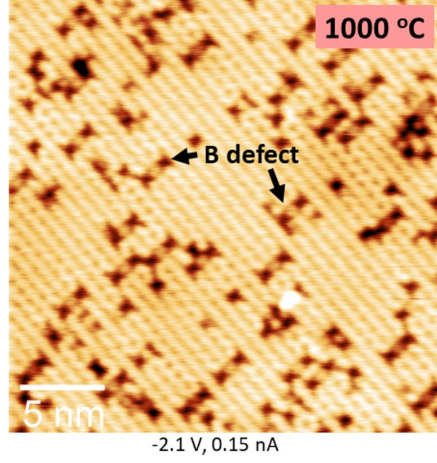


FIG. 5. Filled-state STM images of a Si(100) surface dosed with 1.5 langmuir BCl_3 at room temperature and annealed at 1000 °C for 1 min. Numerous three-dimer-wide “bowtie” defects typical of a highly B-doped substrate⁴⁷ are visible on the surface indicating that B adsorbates have diffused several layers into the surface.

REFERENCES

- ¹D. R. Ward, S. W. Schmucker, E. M. Anderson, E. Bussmann, L. Tracy, T.-M. Lu, L. N. Maurer, A. Baczewski, D. M. Campbell, M. T. Marshall, and S. Misra, “Atomic precision advanced manufacturing for digital electronics,” *Electronic Device Failure Analysis* **22**, 4–11 (2020).
- ²E. Bussmann, R. E. Butera, J. H. Owen, J. N. Randall, S. M. Rinaldi, A. D. Baczewski, and S. Misra, “Atomic-precision advanced manufacturing for si quantum computing,” *MRS Bulletin* , 1–9 (2021).
- ³A. A. Khajetoorians, D. Wegner, A. F. Otte, and I. Swart, “Creating designer quantum states of matter atom-by-atom,” *Nature Reviews Physics* **1**, 703–715 (2019).
- ⁴Y.-P. Shim and C. Tahan, “Bottom-up superconducting and josephson junction devices inside a group-iv semiconductor,” *Nature communications* **5**, 1–8 (2014).
- ⁵T. V. Pavlova, G. M. Zhidomirov, and K. N. Eltsov, “First-principle study of phosphine adsorption on si(001)-2×1-cl,” *The Journal of Physical Chemistry C* **122**, 1741–1745 (2018).
- ⁶K. J. Dwyer, M. Dreyer, and R. E. Butera, “Stm-induced desorption and lithographic patterning of cl-si(100)-(2×1),” *The Journal of Physical Chemistry A* **123**, 10793–10803 (2019).
- ⁷T. Pavlova and K. Eltsov, “Reactivity of the si (100)-2×1-cl surface with respect to ph₃, pcl₃, and bcl₃: Comparison with ph₃ on si(100)-2×1-h,” *Journal of Physics: Condensed Matter* (2021).
- ⁸J. Lyding, T.-C. Shen, J. Hubacek, J. Tucker, and G. Abeln, “Nanoscale patterning and oxidation of h-passivated si(100)-2×1 surfaces with an ultrahigh vacuum scanning tunneling microscope,” *Applied physics letters* **64**, 2010–2012 (1994).
- ⁹J. Randall, J. Lyding, S. Schmucker, J. Von Ehr, J. Ballard, R. Saini, H. Xu, and Y. Ding, “Atomic precision lithography on si,” *Journal of Vacuum Science & Technology B: Microelectronics and Nanometer Structures Processing, Measurement, and Phenomena* **27**, 2764–2768 (2009).
- ¹⁰J. G. Keizer, S. Koelling, P. M. Koenraad, and M. Y. Simmons, “Suppressing segregation in highly phosphorus doped silicon monolayers,” *ACS nano* **9**, 12537–12541 (2015).

- ¹¹S. R. Schofield, N. J. Curson, M. Y. Simmons, F. J. Rueß, T. Hallam, L. Oberbeck, and R. G. Clark, “Atomically precise placement of single dopants in Si,” *Physical Review Letters* **91**, 136104 (2003).
- ¹²L. Oberbeck, N. J. Curson, T. Hallam, M. Y. Simmons, G. Bilger, and R. Clark, “Measurement of phosphorus segregation in silicon at the atomic scale using scanning tunneling microscopy,” *Applied Physics Letters* **85**, 1359–1361 (2004).
- ¹³F. J. Rueß, W. Pok, T. C. Reusch, M. J. Butcher, K. E. J. Goh, L. Oberbeck, G. Scappucci, A. R. Hamilton, and M. Y. Simmons, “Realization of atomically controlled dopant devices in silicon,” *Small* **3**, 563–567 (2007).
- ¹⁴T. Škřeň, S. A. Köster, B. Douhard, C. Fleischmann, and A. Fuhrer, “Bipolar device fabrication using a scanning tunnelling microscope,” *Nature Electronics* , 1–7 (2020).
- ¹⁵R. Ruskov and C. Tahan, “On-chip cavity quantum phonodynamics with an acceptor qubit in silicon,” *Physical Review B* **88**, 064308 (2013).
- ¹⁶J. Salfi, M. Tong, S. Rogge, and D. Culcer, “Quantum computing with acceptor spins in silicon,” *Nanotechnology* **27**, 244001 (2016).
- ¹⁷J. Salfi, J. A. Mol, D. Culcer, and S. Rogge, “Charge-insensitive single-atom spin-orbit qubit in silicon,” *Physical review letters* **116**, 246801 (2016).
- ¹⁸E. Bustarret, C. Marcenat, P. Achatz, J. Kačmarčík, F. Lévy, A. Huxley, L. Ortéga, E. Bourgeois, X. Blase, D. Débarre, *et al.*, “Superconductivity in doped cubic silicon,” *Nature* **444**, 465–468 (2006).
- ¹⁹J.-E. Duvauchelle, A. Francheteau, C. Marcenat, F. Chiodi, D. Débarre, K. Hasselbach, J. R. Kirtley, and F. Lefloch, “Silicon superconducting quantum interference device,” *Applied Physics Letters* **107**, 072601 (2015).
- ²⁰P. Bonnet, F. Chiodi, D. Flanigan, R. Delagrangé, N. Brochu, D. Débarre, and H. I. Sœur, “Strongly non-linear superconducting silicon resonators,” *arXiv preprint arXiv:2101.11125* (2021).
- ²¹M. S. Radue, S. Baek, A. Farzaneh, K. J. Dwyer, Q. Campbell, A. D. Baczewski, E. Bussmann, G. T. Wang, Y. Mo, S. Misra, and R. E. Butera, “AlCl₃-dosed Si(100)–2×1: Adsorbates, Chlorinated Al Chains, and Incorporated Al,” *J. Phys. Chem. C* , 125–11336 (2021).
- ²²K. J. Dwyer, S. Baek, A. Farzaneh, M. Dreyer, J. R. Williams, and R. E. Butera, “B-doped δ -layers and nanowires from area-selective deposition of bcl₃ on si(100),” *ACS Applied*

- Materials & Interfaces **13**, 41275–41286 (2021).
- ²³J. H. G. Owen, Q. Campbell, R. Santini, J. A. Ivie, A. Baczewski, S. W. Schmucker, E. Bussmann, S. Misra, and J. N. Randall, “Al-alkyls as acceptor dopant precursors for atomic-scale devices,” *Journal of Physics: Condensed Matter* (2021).
- ²⁴J. C. Ho, R. Yerushalmi, Z. A. Jacobson, Z. Fan, R. L. Alley, and A. Javey, “Controlled nanoscale doping of semiconductors via molecular monolayers,” *Nature materials* **7**, 62–67 (2008).
- ²⁵Ye, Liang and González-Campo, Arántzazu and Núñez, Rosario and de Jong, Michel P and Kudernac, Tibor and van der Wiel, Wilfred G and Huskens, Jurriaan, “Boosting the boron dopant level in monolayer doping by carboranes,” *ACS applied materials & interfaces* **7**, 27357–27361 (2015).
- ²⁶D. Silva-Quinones, C. He, R. E. Butera, G. T. Wang, and A. V. Teplyakov, “Reaction of bcl_3 with h-and cl-terminated si(100) as a pathway for selective, monolayer doping through wet chemistry,” *Applied Surface Science* , 146907 (2020).
- ²⁷E. Frederick, Q. Campbell, I. Kolesnichenko, L. F. Peña, E. M. Anderson, A. Benavidez, D. Wheeler, and S. Misra, “Ultradoping boron on si(100) via solvothermal chemistry,” *Chemistry—A European Journal* (2021).
- ²⁸D. Silva-Quinones, R. E. Butera, G. T. Wang, and A. V. Teplyakov, “Solution chemistry to control boron-containing monolayers on silicon: Reactions of boric acid and 4-fluorophenylboronic acid with h-and cl-terminated si(100),” *Langmuir* (2021).
- ²⁹J. A. Ivie, Q. Campbell, J. C. Koepke, M. I. Brickson, P. A. Schultz, R. P. Muller, A. M. Mounce, D. R. Ward, M. S. Carroll, E. Bussmann, *et al.*, “The impact of stochastic incorporation on atomic-precision si: P arrays,” *arXiv preprint arXiv:2105.12074* (2021).
- ³⁰O. Warschkow, N. J. Curson, S. R. Schofield, N. A. Marks, H. F. Wilson, M. W. Radny, P. V. Smith, T. C. Reusch, D. R. McKenzie, and M. Y. Simmons, “Reaction paths of phosphine dissociation on silicon (001),” *Journal of Chemical Physics* **144**, 014705 (2016).
- ³¹P. Giannozzi, S. Baroni, N. Bonini, M. Calandra, R. Car, C. Cavazzoni, D. Ceresoli, G. L. Chiarotti, M. Cococcioni, I. Dabo, A. Dal Corso, S. de Gironcoli, S. Fabris, G. Fratesi, R. Gebauer, U. Gerstmann, C. Gougoussis, A. Kokalj, M. Lazzeri, L. Martin-Samos, N. Marzari, F. Mauri, R. Mazzarello, S. Paolini, A. Pasquarello, L. Paulatto, C. Sbraccia, S. Scandolo, G. Sclauzero, A. P. Seitsonen, A. Smogunov, P. Umari, and R. M. Wentzcovitch, “QUANTUM ESPRESSO: a modular and open-source software project for quantum

- simulations of materials,” *Journal of Physics: Condensed Matter* **21**, 395502 (2009).
- ³²M. J. van Setten, M. Giantomassi, E. Bousquet, M. J. Verstraete, D. R. Hamann, X. Gonze, and G. M. Rignanese, “The PSEUDODOJO: Training and grading a 85 element optimized norm-conserving pseudopotential table,” *Computer Physics Communications* **226**, 39–54 (2018), arXiv:1710.10138.
- ³³J. P. Perdew, K. Burke, and M. Ernzerhof, “Generalized Gradient Approximation Made Simple,” *Physical Review Letters* **77**, 3865–3868 (1996).
- ³⁴H. J. Monkhorst and J. D. Pack, “Special points for brillouin-zone integrations,” *Physical review B* **13**, 5188 (1976).
- ³⁵A. Bortz, M. Kalos, and J. Lebowitz, “A New Algorithm for Monte Carlo Simulation of Ising Spin Systems,” *Journal of Computational physics* **17**, 10–18 (1975).
- ³⁶D. T. Gillespie, “A general method for numerically simulating the stochastic time evolution of coupled chemical reactions,” *Journal of Computational Physics* **22**, 403–434 (1976).
- ³⁷M. Leetmaa and N. V. Skorodumova, “KMCLib: A general framework for lattice kinetic Monte Carlo (KMC) simulations,” *Computer Physics Communications* **185**, 2340–2349 (2014).
- ³⁸S. Arrhenius, “Uber die reaktionsgeschwindigkeit bei der inversion von rohrzucker durch sauren,” *Zeitschrift für Physikalische Chemie* **4**, 226 (1889).
- ³⁹“Kinetic monte carlo code,” online.
- ⁴⁰D. Nečas and P. Klapetek, “Gwyddion: an open-source software for spm data analysis,” *Open Physics* **10**, 181–188 (2012).
- ⁴¹Q. Campbell, J. A. Ivie, E. Bussmann, S. W. Schmucker, A. D. Baczewski, and S. Misra, “A model for atomic precision p-type doping with diborane on si(100)–2×1,” *The Journal of Physical Chemistry C* **125**, 481–488 (2021).
- ⁴²M. S. Radue, R. Butera, and Y. Mo, “Dopant precursor adsorption into single-dimer windows: Towards guided self-assembly of dopant arrays on si(100),” *Chemical Physics Letters* , 139258 (2021).
- ⁴³G. A. Ferguson, U. Das, and K. Raghavachari, “Interaction of lewis acids with si (100)–2×1 and ge(100)–2×1 surfaces,” *The Journal of Physical Chemistry C* **113**, 10146–10150 (2009).
- ⁴⁴J. Ferguson, A. Weimer, and S. George, “Atomic layer deposition of boron nitride using sequential exposures of bcl₃ and nh₃,” *Thin Solid Films* **413**, 16–25 (2002).

- ⁴⁵S. Consiglio, R. D. Clark, D. O'Meara, C. S. Wajda, K. Tapily, and G. J. Leusink, "Comparison of b_2o_3 and bn deposited by atomic layer deposition for forming ultrashallow dopant regions by solid state diffusion," *Journal of Vacuum Science & Technology A: Vacuum, Surfaces, and Films* **34**, 01A102 (2016).
- ⁴⁶A. Pilli, J. Jones, V. Lee, N. Chugh, J. Kelber, F. Pasquale, and A. LaVoie, "*In situ* xps study of low temperature atomic layer deposition of b_2o_3 films on si using bcl_3 and h_2o precursors," *Journal of Vacuum Science & Technology A: Vacuum, Surfaces, and Films* **36**, 061503 (2018).
- ⁴⁷Z. Liu, Z. Zhang, and X. Zhu, "Atomic Structures of Boron-Induced Protrusion Features on Si(100) Surfaces," *Phys. Rev. B* **77**, 035322 (2008).
- ⁴⁸A. Agrawal, R. E. Butera, and J. H. Weaver, "Cl insertion on si(100)-(2 \times 1): Etching under conditions of supersaturation," *Phys. Rev. Lett.* **98**, 136104 (2007).
- ⁴⁹Z. Zhang, M. A. Kulakov, B. Bullemer, I. Eisele, and A. V. Zotov, "Epitaxial Growth of Ultrathin Si Caps on Si(100): B Surface Studied by Scanning Tunneling Microscopy," *Appl. Phys. Lett.* **69**, 494–496 (1996).
- ⁵⁰A. Otero-de-la Roza, E. R. Johnson, and V. Luaña, "Critic2: A program for real-space analysis of quantum chemical interactions in solids," *Computer Physics Communications* **185**, 1007–1018 (2014).